Reprinted from JOURNAL OF THE ATMOSPHERIC SCIENCES, Vol. 52, No. 12, 15 June 1995
American Meteorological Society

The Gravity Wave Response above Deep Convection in a Squall Line Simulation

M. J. ALEXANDER, J. R. HOLTON, AND D. R. DURRAN

The Gravity Wave Response above Deep Convection in a Squall Line Simulation

M. J. ALEXANDER, J. R. HOLTON, AND D. R. DURRAN

Department of Atmospheric Sciences, University of Washington, Seattle, Washington

(Manuscript received 6 April 1994, in final form 19 December 1994)

ABSTRACT

High-frequency gravity waves generated by convective storms likely play an important role in the general circulation of the middle atmosphere. Yet little is known about waves from this source. This work utilizes a fully compressible, nonlinear, numerical, two-dimensional simulation of a midlatitude squall line to study vertically propagating waves generated by deep convection. The model includes a deep stratosphere layer with high enough resolution to characterize the wave motions at these altitudes. A spectral analysis of the stratospheric waves provides an understanding of the necessary characteristics of the spectrum for future studies of their effects on the middle atmosphere in realistic mean wind scenarios. The wave spectrum also displays specific characteristics that point to the physical mechanisms within the storm responsible for their forcing. Understanding these forcing mechanisms and the properties of the storm and atmosphere that control them are crucial first steps toward developing a parameterization of waves from this source. The simulation also provides a description of some observable signatures of convectively generated waves, which may promote observational verification of these results and help tie any such observations to their convective source.

1. Introduction

Vertically propagating gravity waves are known to have a profound effect on the structure and circulation of the middle atmosphere. Gravity wave drag and diffusion, for example, are fundamental in reconciling middle atmosphere heating rates with observed zonal-mean winds and temperatures (Holton 1983) and play an important role in determining chemical composition in the mesosphere (Garcia and Solomon 1985). In addition, gravity wave drag may drive the semiannual oscillation observed near the equatorial mesopause (Dunkerton 1982) and may contribute to the forcing of the quasi-biennial oscillation (Takahashi and Boville 1992).

The zonal-mean effects described above have been deduced from parameterizations using crude assumptions about the characteristic scales and phase speeds of the gravity wave spectrum and employ empirical "efficiency factors" to account for assumed irregularities in the temporal and spatial distributions of wave activity. Three-dimensional general circulation models (GCMs) are, however, sensitive to the details of the geographical and temporal distributions of wave activity and so require a more detailed description of the gravity waves and their sources. Fairly successful parameterizations of orographically forced gravity waves meeting these new requirements have been developed by McFarlane (1987), Palmer et al. (1986), and Bacmeister (1993). However other important gravity wave sources—convection, shear, fronts, and geostrophic adjustment—are too poorly understood to be easily parameterized in this way, although one attempt has been made to include these effects in a GCM (Rind et al. 1988).

Convective activity in particular is ubiquitous, and observations suggest it to be at least equally as important as topographic forcing (Fritts and Nastrom 1992) and possibly the most important source in the Tropics and Southern Hemisphere. Although gravity wave power spectra derived from observations display the dominance of long-period planetary-scale waves, it is the high-frequency waves that carry much of the energy and momentum fluxes (Fritts and Vincent 1987; Bergman and Salby 1994) and may be the most important for propagation to mesospheric altitudes. This underscores the need to include nonstationary waves from sources like convective activity in global models.

The forcing mechanisms responsible for generating vertically propagating waves in convective clouds are not well understood. Fovell et al. (1992, hereafter FDH) demonstrated the "mechanical oscillator effect," oscillating updrafts and downdrafts impinging on the tropopause, as a mechanism for generating high-frequency waves in multicell storms. Convective turrets penetrating into an overlying shear layer can also excite waves in a process analogous to orographic forcing. Pfister et al. (1993b) explained wind variations above a convective turret with a model of a slowly

Corresponding author address: Dr. M. Joan Alexander, Department of Atmospheric Sciences, AK-40, University of Washington, Seattle, WA 98195.

moving transient obstacle in a mean wind, similar to the mechanical oscillator effect; but this disturbance was much larger in scale than considered here. Wave excitation by a transient or steady heat source in a stratified atmosphere is another forcing mechanism (Pandya et al. 1993; Nicholls et al. 1991; Lin and Smith 1986), and certain aspects of this problem can be described via simple analytical models. Understanding the wave forcing mechanisms active in convection, as well as the properties of the storm and atmosphere that control the wave characteristics, are crucial steps toward developing a parameterization of their global effects on the middle atmosphere.

To begin to characterize waves generated by deep convection, we utilize a numerical mesoscale simulation of a squall line with a deep stratospheric layer and high enough spatial and temporal resolution to resolve the gravity wave motions. The model is two-dimensional and utilizes a midlatitude thermodynamic sounding and stratospheric winds that are constant in height. Although these specific features of the model are not the most general, an understanding of the wave forcing mechanisms and the parameters responsible for shaping the characteristics of the gravity wave response can potentially be applied to the much more general problem of waves forced by deep convection as it occurs around the globe. With the tools of spectral analysis, we characterize the stratospheric waves produced in the simulation. We then examine the spectral properties of the stratospheric waves using the linear gravity wave dispersion relation coupled to knowledge of the properties of the storm motions to relate the wave characteristics to the forcing mechanisms active in the troposphere. These results provide a coherent picture of the wave forcing–response relationships and allow us to make some general statements regarding gravity waves forced by deep convection.

A few observations of stratospheric waves generated by convection exist in the literature, but none provide a general description of waves from this source. Larsen et al. (1982) observed stratospheric wave motions above convection and only when cloud heights reached the level of the tropopause. In the case they highlighted, a high-frequency wave with a period of 6 min and vertical wavelength of 7 km was observed. The MU radar observations in Sato (1993) find strong short-period gravity waves with high aspect ratios ($k/m \sim 1$) in the stratosphere above deep convection before the passage of a typhoon. VHF radar wind observations in Lu et al. (1984) showed significant enhancements in variance associated with thunderstorms at periods between 10 min and 6 h in the troposphere but not at stratospheric levels. Pfister et al. (1986, 1993a,b) utilized aircraft measurements in the tropical lower stratosphere to identify large amplitude wave features, associated with outbreaks of convection, with horizontal wavelengths in the 5–110 km range. This important work characterized specific wave features in a few case studies, though no general or spectral descriptions of convectively generated waves have yet emerged from such observations. Radar wind profiler measurements of Balsley et al. (1988) revealed a signature of downward vertical winds near the tropopause during periods of heavy rainfall. Although the origin of this feature is still being debated, our results relate this observed structure in the wind profile to a persistent low-frequency gravity wave motion in our numerical simulation. In addition, our results predict other characteristic features of convectively generated gravity waves that may be observable by ground-based radar. Future work will focus on the effects of momentum and energy transport by convectively generated waves on the middle atmosphere. In this paper, we seek to relate the stratospheric waves to their tropospheric forcing mechanisms and to describe observable characteristics of waves generated by convection for the purpose of stimulating verification of the results via observation.

An overview of the squall line simulation follows in section 2, as well as a more detailed look at some of the storm organization characteristics in the troposphere. Section 3 describes the spectral analysis results. In section 4, a coherent physical interpretation of the results of the spectral analysis is developed. Using the linear dispersion relation for internal gravity waves, the characteristics of the stratospheric wave field are described and related to specific tropospheric forcing mechanisms. A discussion of the relationship between the nature of the forcing and some fundamental properties of the storm follows in section 5 and provides some insight into the generality of these results as a model of wave generation by deep convection. Some predicted observables of the wave characteristics in the model are also highlighted, as well as a description of future work necessary to test the generality of the conclusions.

2. The squall line simulation

a. General model description

The squall line simulation discussed in this paper is very similar to work described in Fovell et al. (1992) and Holton and Durran (1993). We will briefly summarize the model characteristics and point out differences from this previous work where appropriate. The model is a two-dimensional simulation of a long-lived squall line utilizing the midlatitude tropospheric sounding of Weisman and Klemp (1982). This sounding is conditionally unstable and produces steady convection following initiation with a 2 K warm bubble near the surface. The model domain size is 840 km in the horizontal and 32 km in the vertical. Horizontal resolution is constant at 1.5 km, and vertical resolution varies with height from 0.5 km near the surface to 0.2 km at the upper boundary in the middle stratosphere. The high resolution in the stratosphere is designed to resolve

some features of wave breaking. Parameterized subgrid-scale mixing is described in Durran and Klemp (1983). It becomes important in regions of strong shear and tends to be quite small in the stratosphere, except in very limited regions where waves approach breaking amplitudes. The upper and lateral radiation boundary conditions have the same form as those in Holton and Durran (1993), with the effective phase speeds at the left and right lateral boundaries chosen at -50 and 35 m s^{-1}, respectively. Durran et al. (1993) describe the efficacy of this lateral boundary condition for cloud models. The upper-boundary radiation condition is that used in Holton and Durran (1993) and described in detail in Durran (1994). This change in the upper-boundary condition allowed removal of the sponge layer employed in FDH.

The model is designed to accurately simulate the dynamics of deep convection to study the generation of buoyancy waves in such systems. The dynamical treatment, including the effects of compressible and nonhydrostatic motions, is fairly sophisticated, while the microphysical treatment is comparatively simple. Ice microphysics and radiative processes are both neglected. The parameterizations and the numerical solution methods are described in detail in Durran and Klemp (1983). The governing equations are described in FDH.

The basic state is the same as the FDH case S(0) and is plotted in Fig. 1 with solid lines. There is moderate shear in the lowest 2.5 km overlain by a layer of weaker shear in the troposphere, a case that Rotunno et al. (1988) found can be well represented by two-dimensional models. Above the tropopause, winds are constant with height at 16 m s^{-1}. The model domain translates eastward at a constant speed of 16 m s^{-1} as well, so the stratospheric waves in the simulation are viewed in the "intrinsic" frame of reference (i.e., observed phase speeds in the stratosphere equal intrinsic phase speeds). The storm also propagates at an average of about 15 m s^{-1}, so it is approximately stationary in the moving frame. Note that the absence of wind shear at the tropopause precludes the forcing of waves in the lower stratosphere via the "obstacle effect" of penetrating turrets into a mean wind at those heights. The constant 16-m s^{-1} wind in the stratosphere, however, allows us to examine the spectral properties of the stratospheric waves without height-dependent Doppler shifting. Results can subsequently be used as input to a linear wave propagation analysis with variable mean winds.

The simulation was run out to 7 h, and diagnostic field variables were saved at 2-min intervals between 3 and 7 h when the convection had developed into a fairly steady mature storm phase. Since the intrinsic frequency of the internal gravity wave motions cannot exceed the buoyancy frequency, this temporal resolution resolves even the highest-frequency gravity wave oscillations in the stratosphere. Also shown in Fig. 1 are the storm-modified profiles (averaged over time and horizontal distance) of zonal wind and buoyancy frequency. The central updraft in the storm center and resulting shear in the horizontal winds create a very different local environment, to which small-scale gravity wave motions may be sensitive. Enhanced shear and decreased stability in the upper troposphere, in particular, may act as efficient filters of any waves forced at lower levels. The stratospheric mean state, on the other hand, remains nearly unperturbed. (Deviations in the stratospheric winds in Fig. 1a can largely be explained by longer wavelength perturbations, which extend be-

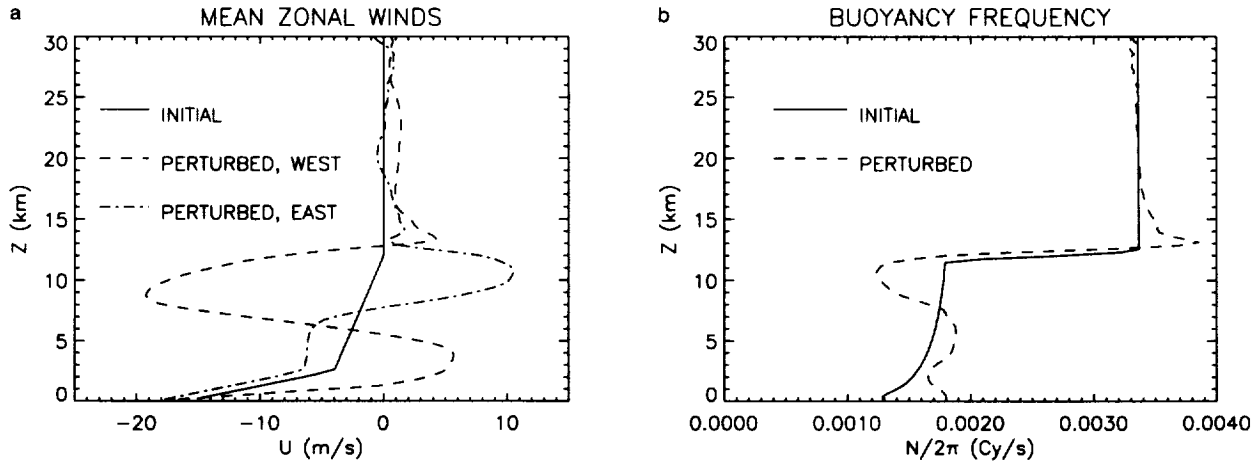

FIG. 1. Zonal average profiles. (a) Horizontal winds for initial conditions (solid line) and in the mature storm. Long dashed line shows the average taken to the west of storm center and the dash-dotted line to the east. These are averaged over 1 h (hours 4–5) and 240 km west and east of the storm center. The mature phase profiles describe the storm-modified mesoscale structure, which may effect wave propagation. (b) Buoyancy frequency (cycles s^{-1}) for the initial conditions (solid line) and in the mature storm (dashed line) averaged over 1 h and over 550 km. (Profiles west and east of storm center are not markedly different.)

yond the side boundaries. Then averaging over an incomplete cycle of the perturbation skews the average.)

A snapshot of the full (x, z) domain at 4 h is shown in Fig. 2. Shading represents vertical velocity contours, thin black lines are surfaces of constant potential temperature, and the heavy contour represents the cloud outline. Wave motions are evident throughout the troposphere and stratosphere. The stratospheric wave field is quite complex; with a primary source associated with the strong central updraft core of the storm, and secondary wave sources associated with propagating cells, which are characterized by strong vertical motions in the upper troposphere to the west of the center of the storm.

Nonlinear instability is controlled in the model by inclusion of biharmonic diffusion in the horizontal and vertical. Unfortunately, the horizontal smoothing coefficients used by Holton and Durran (1993) and FDH were found to seriously damp waves of horizontal wavelengths less than ~20 km (i.e., $\sim 12\Delta x$). To improve the simulation of shorter waves, the horizontal smoothing coefficient was reduced by a factor of 3 (from that used in Holton and Durran) for this study. The effects of the smoothing will be described further via spectral analysis in section 3. Compared to FDH's S(0) case (their Fig. 5, lower panel), Fig. 2 shows short horizontal-scale waves are emphasized over the longer wavelength waves in the western wave fan pattern. This is the result of the decreased smoothing coefficient that allows the convection to organize in a stronger, narrower updraft.

Figure 3 shows a close-up view of the time-averaged winds in the central updraft region of the troposphere. The mature storm is characterized by a strong central updraft tilting rearward with height, which Rotunno et al. (1988) describe in terms of a competition between

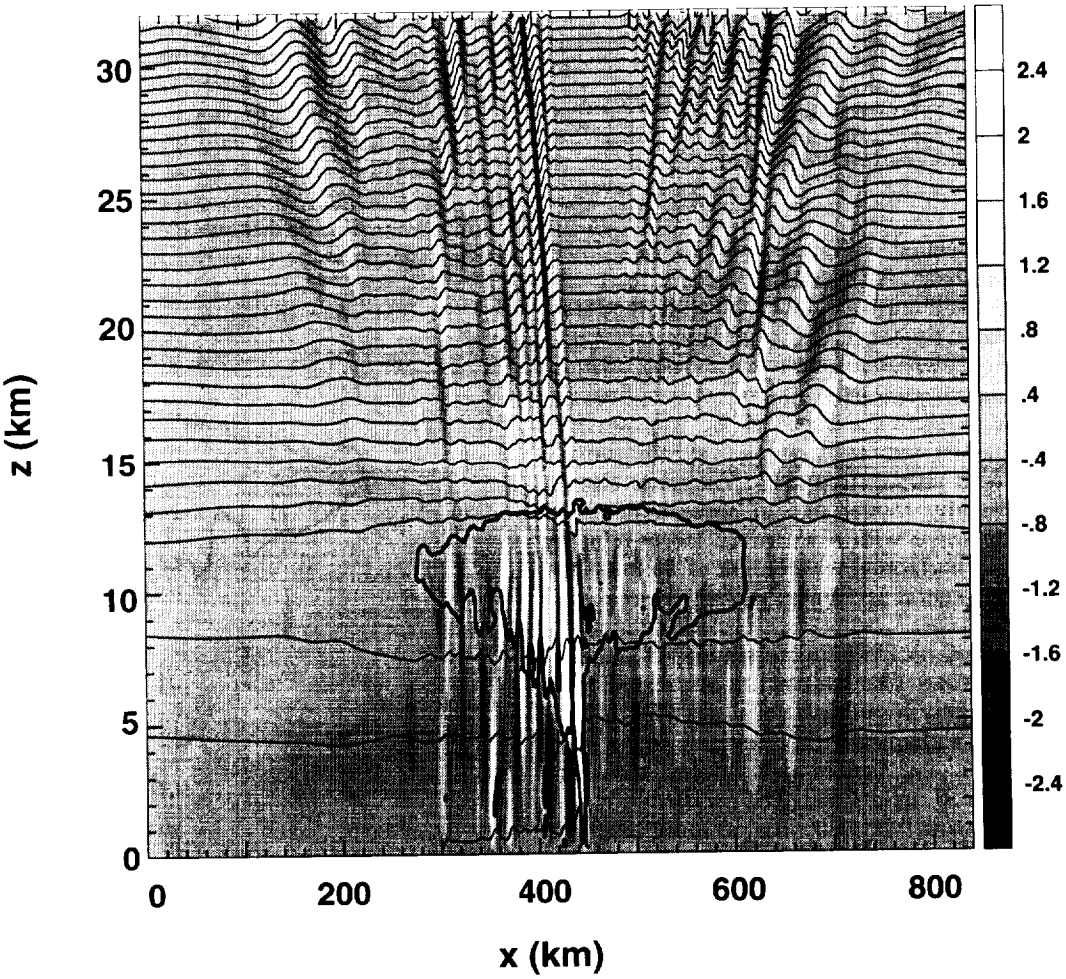

FIG. 2. The squall line simulation at 4 h of simulation time. Shading represents contours of vertical velocity. (Contrast has been enhanced to show the qualitative structure; the full range of vertical velocities is +20 to −5 m s^{-1}.) Thin lines are isentropes (at 15-K intervals), and the thick line shows the cloud outline (cloud water mixing ratio = 1×10^{-4} g g^{-1}). The tropopause is at 12–13 km.

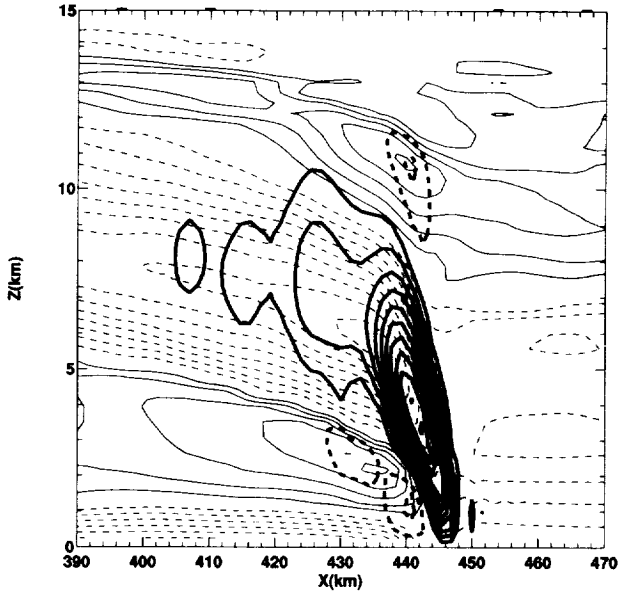

FIG. 3. Steady structure of the tropospheric winds relative to the 16 m s^{-1} moving-reference frame in the vicinity of the central updraft. Thin lines are contours of horizontal velocity at 3 m s^{-1} intervals. Thick lines show vertical velocity at 1 m s^{-1} intervals. These are 1-h averages (hours 4–5) to show the steady storm characteristics. Solid contours show positive velocities (eastward/upward), and dashed contours negative (westward/downward).

the vorticity associated with cold pool buoyancy and low-level wind shear. A balance of these effects can give the upward and rearward tilt of the updraft, which produces a long-lived storm. This orientation of the updraft preferentially produces the rearward propagating convective cells characteristic of multicell mesoscale storms. Figure 4 shows a view of the tropospheric storm center and the numerical analog to a trailing stratiform region with propagating cells. Yang and Houze (1994) successfully model one of these cells as a trapped gravity wave with a westward storm-relative phase speed and horizontal wavelength of 16 km. Our simulation is in general agreement with these results of Yang and Houze.

The peak updraft oscillates in magnitude and altitude as a function of time. Oscillations are associated with the formation of new convective cells (see FDH). The oscillations have a characteristic frequency in the simulation; however, the factors determining that frequency are not well understood. The oscillation in the present simulation will be described in more detail in section 4. The frequency of this oscillation will be shown to determine the characteristics of a certain fraction of the stratospheric waves produced in the model.

b. Observable signatures of the convectively generated wave field

The structure of the time-averaged wind shown in Fig. 3 reveals an observed, but previously unexplained, feature in the vertical velocity profile above the central convective updraft region near the tropopause. Balsley et al. (1988), using a radar wind profiler, observed persistent downward velocities near tropopause altitudes during periods of heavy rainfall associated with the convective regions of mesoscale storms. They averaged 1-h periods of data and report downward velocities of ~0.1 m s^{-1} near the tropopause, in their observations of tropical storms. To compare with their result (Fig. 3 of Balsley et al. 1988), the storm center winds must be averaged temporally (1-h periods) as well as horizontally (60 km) to account for the motion of the storm (~15 m s^{-1}) relative to a ground-based observer during the 1-h period. The result is shown in Fig. 5. The amplitudes of both the convective updraft and mysterious downdraft feature match the results of Balsley et al. very closely. The altitudes differ because the comparison is between a midlatitude simulation and tropical observations, but both show the downdraft peaking very near the level of the tropopause. MU radar observations reported in Sato (1993) also reveal strikingly similar observations of the vertical velocity field above the strong convective updraft within Typhoon Kelly.

Our convection simulation resolves this downdraft feature both in time and space and provides the relationship of the vertical velocity to other dynamically important fields. In Fig. 3, it can be seen that the downdraft is associated with eastward horizontal velocity perturbations. Figure 6 shows a horizontal cross section of the vertical velocity in the downdraft region as a

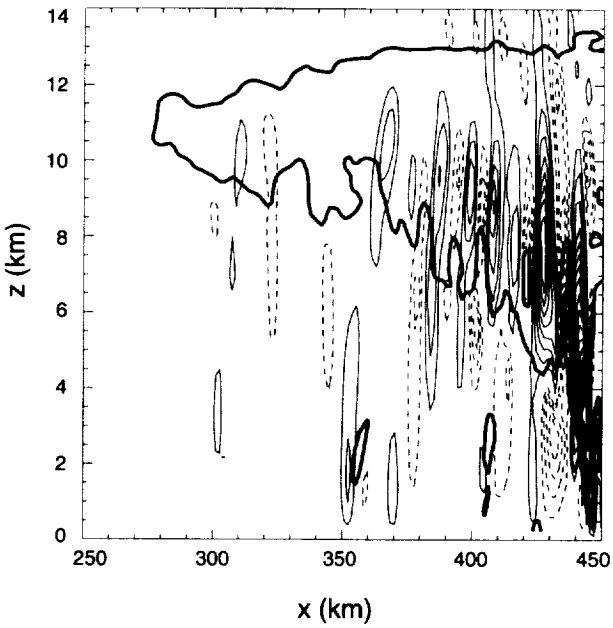

FIG. 4. Vertical velocity contours (thin lines) at t = 4 h in the trailing region west of the storm showing propagating convective cells. The contour interval is 1 m s^{-1}. Dashed contours represent negative velocities. The heavy line is the cloud boundary.

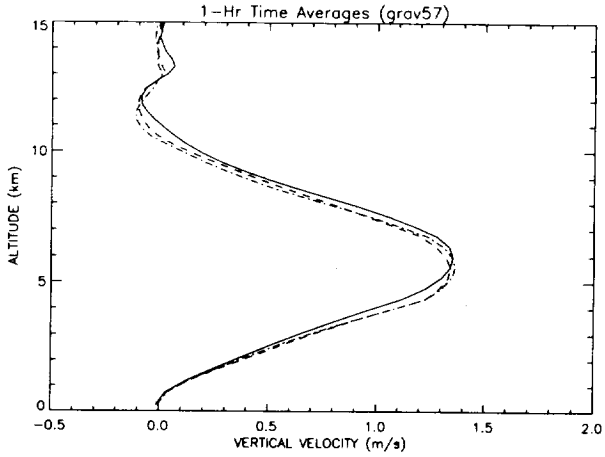

FIG. 5. One-hour averages of vertical velocity profiles in the vicinity of the main updraft of the storm. Averages are over hours 4–5 (solid), 5–6 (dashed), and 6–7 (dash-dotted). Averaging over 60 km in x was also necessary for comparison with Balsley et al. (1988, their Fig. 3) to account for the storm motion in their ground-based observations (see text). These results show striking similarity in both form and magnitude to the Balsley et al. profiles.

function of time at z = 11.2 km. The quasi-steady nature of the downdraft is modulated by the oscillations associated with the formation of new cells, which can be observed in Fig. 6 as propagating features with high negative phase speeds. The downdraft feature, however, persists throughout the 4 h of simulation, propagating from x = 448 km to x = 434 km over this period, making it approximately stationary relative to the storm (which drifts rearward at the same 1 m s^{-1} rate in the 16 m s^{-1} moving frame).

Autocorrelation of the vertical velocity, $w(x)$ at z = 11.2 km, averaged over the half-hour period of hours 5.9–6.4, reveals a 12-km horizontal wavelength signature (Fig. 7, solid line). This time period was chosen because the feature is fairly unperturbed by the weaker storm oscillations during this period. Cross correlation of $w(x)$ and the potential temperature $\theta(x)$ in the same period reveals these to be highly correlated and exactly 1/4 wavelength out of phase (Fig. 7, dashed line). The relationships of the w, θ, and u fields suggest the downdraft is simply a characteristic of a gravity wave motion. The forcing mechanism is likely related to convective updraft penetration above the level of neutral buoyancy. This low-frequency wave in the upper troposphere may be a signature of long-lived deep convection that penetrates to levels near the tropopause.

In the stratosphere, a second observable feature of the storm-generated gravity waves is the asymmetry in the momentum flux east and west of the center of the storm. This can be thought of as a natural consequence of the storm center ultimately being the energy source for all the waves. Wave momentum flux $\rho_0 u'w'$ is negative everywhere west of storm center and positive everywhere east of storm center. This is demonstrated in Fig. 8, which shows a 1-h time average of the stratospheric momentum flux as a function of altitude and distance from the center of the storm. Peak magnitudes in the west are much larger than in the east and are concentrated just behind the storm center, where the highest-frequency waves (those with the most vertically oriented lines of constant phase) are found. These waves are absent in the eastern half of the domain in accord with the results of FDH, if the high frequency waves are associated with a mechanical pumping forcing mechanism. The eastern momentum flux is all associated with waves generated in the early stages of the simulation before the storm matures. Absence of any appreciable flux near storm center on the eastern half

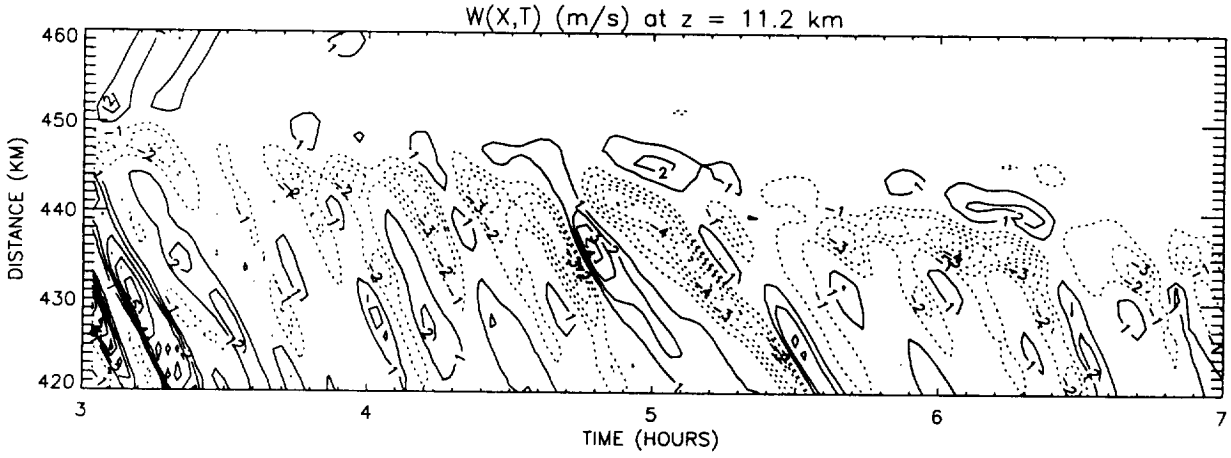

FIG. 6. Horizontal cross section of the vertical velocity at z = 11.2 km as a function of time. The position is just above the central updraft where the steady negative velocities are observed. The downdraft drifts slowly westward (at ~1 m s^{-1}) in the moving frame, closely following the motion of the storm. The downward velocity signature is modulated by the storm oscillations (see section 4) and production of new cells, which can be seen propagating to the west with large negative phase speeds.

demonstrates the absence of eastward propagating wave forcing in the mature storm.

With the technique developed in Vincent and Reid (1983), the asymmetry in the momentum flux field (Fig. 8) ahead of and behind the storm may be observable by ground-based radar. The long integration times required for these determinations may dilute the magnitude of the observed momentum fluxes, but the change in sign as the storm passes overhead may be an observable signature in the stratospheric wind perturbations that could help tie them to their convective source. This would provide an important verification of the results of the simulation.

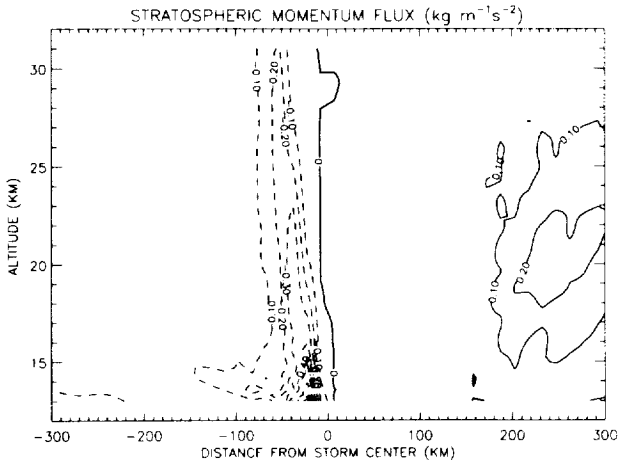

FIG. 8. Wave momentum flux $\rho_0 u'w'$ in the stratosphere, averaged over 1-h of simulation time (hours 4–5). Evidence of penetrative convection can be seen at z = 13 km and x = −20 km. Elsewhere, peak magnitudes are in the west at −0.3 to −0.4 kg m^{-1} s^{-2}, associated with high-frequency westward-propagating waves. Note the asymmetry in sign of the momentum flux east and west of storm center.

3. Spectral analysis

a. *Method of power spectrum estimation*

To characterize the spectral properties of the waves produced in the simulation, a fast Fourier transform is performed on the vertical velocity field, and the periodogram method (Press et al. 1989) is used to estimate the one-sided power spectral density (PSD). The spectra herein are normalized such that the integral of the spectrum over the frequency–wavenumber domain gives the power in the original signal averaged over the time–space domain. [This normalization corresponds to "form (b)" in Percival and Walden (1993, p. 111).] Prior to computing the Fourier transform, the original series is first detrended by subtraction of a least-squares straight-line fit, and a Welch window function is also applied to reduce the spectral leakage in the 1D PSD estimate. (Note that the subtracted linear fit is quite small. Also, the Welch taper function primarily affects the spectra by reducing the noise at the very low power end of the spectrum by reducing the spectral leakage associated with the periodogram estimate.) Fourier transforms are computed using the Numerical Recipes (Press et al. 1989) FOUR1 and FOURN subroutines.

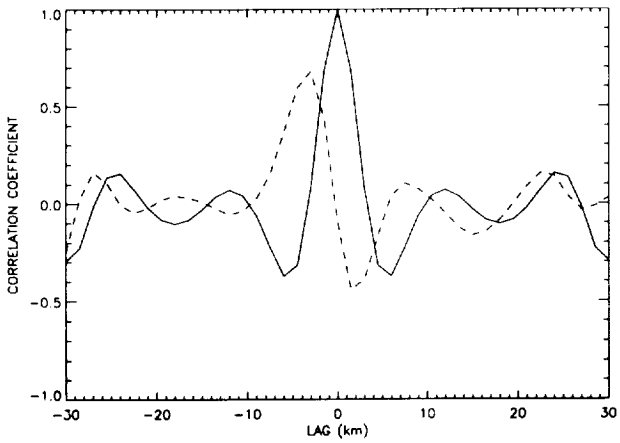

FIG. 7. Autocorrelation of $w(x)$ shown in Fig. 6 (solid line) at z = 11.2 km reveals a 12-km horizontal wavelength signature associated with the stationary downdraft feature. Cross correlation of $w(x)$ and $\theta(x)$ (dashed line) shows a strong correlation with a 1/4 cycle phase lag relationship (w lags θ in x by 3 km = $\lambda_x/4$). Both correlations have been averaged over the half-hour period of hours 5.9–6.4, where the downdraft appears steadily (is least interrupted by the storm oscillations) at this altitude.

The main updraft within the storm cloud, as well as the propagating convective cells, are fueled by latent heating and are largely confined to the troposphere below the level of neutral buoyancy. Above the tropopause, motions are predominantly associated with freely vertically propagating waves. We therefore split the analysis of the model domain at the tropopause, which can be thought of as a separation of the forcing region below and response region above, for vertically propagating waves generated by convection. The analysis of the stratospheric portion of the simulation is further split into two halves, west and east of storm center. This separation approximates the separation of the wave field into westward (rearward) and eastward (forward) propagating waves (see Fig. 8).

Vertical wavenumber spectra are computed at each time t and each horizontal grid point x over the 13–32-km altitude interval, resolving vertical wavelengths of 0.7–19.0 km (wavenumbers[1] 5.3 × 10^{-5} to 1.4 × 10^{-3} Cy m^{-1}). To reduce the uncertainty inherent in

[1] Note that wavenumbers given here are in units of cycles per meter (Cy m^{-1}), and frequencies in cycles per second (Cy s^{-1}); that is, k = 1 λ_x^{-1}, m = 1 λ_z^{-1}, and ω = (period)$^{-1}$, with no factor of 2π. This makes conversions to wavelength and period a bit simpler and allows direct comparison with most published spectra derived from observations.

the periodogram power spectrum estimate, the spectra are averaged in x and t. (Western and eastern halves of the domain are averaged separately.) The averaging allows comparison of these results with spectra in horizontal wavenumber and frequency over the same domain in (x, z, t) and also reduces the variance associated with the statistical uncertainty in the PSD estimate, so that the standard deviation is reduced to 0.6%.

In the absence of vertical shear of the mean wind, the amplitudes of the perturbation fields (e.g., vertical velocity) in linear gravity waves vary with altitude as the inverse square root of the basic-state density field. To correct for this effect, before computing the spectrum, amplitudes are first normalized by division of the exponential growth rate factor, $\exp[(z - z_0)/2H]$ with $z_0 = 13$ km and $H = 7$ km. This prevents biasing the results toward the spectral properties at the highest altitudes. The spectral magnitudes then represent wave amplitudes at the 13-km altitude. (Note that the removal of this vertical growth rate has little effect on the shape of the resulting spectrum but, primarily, reduces only the magnitude. Normalization to 13 km produces a spectrum that can be used in subsequent analyses to study linear propagation to greater heights.)

Frequency spectra are similarly computed at each spatial position for the interval 3–7 h of simulation time resolving waves with periods between 4 min and 4 h. Spectra are then averaged in x (maintaining the west–east distinction) and in z (first normalizing to $z = 13$ km with the square of the above exponential growth rate factor). The averaging reduces the uncertainty in the resulting spectral estimates to 0.7%.

Horizontal wavenumber spectra are computed at each altitude and each time over a 384-km interval west and then east of storm center, resolving horizontal wavelengths between 3 and 384 km. Averaging in t and z as described above reduces the uncertainty in the spectral estimates to 1.0%.

Spectra in two dimensions can also be computed from the squall line simulation results. As will be seen in section 3b, resolution of the stratospheric waves only warrants this for the $(x, t) \rightarrow (k, \omega)$ domains. Two-dimensional spectra are computed at each altitude level in the 13–32-km altitude range of the model and then averaged as described for the one-dimensional ω and k spectra, reducing the uncertainty in the PSD estimate to 11%.

b. *Results of the spectral analysis of the vertical velocity field*

The following analysis of the vertical velocity field $w(x, z, t)$ from the squall line simulation provides a description of the stratospheric wave field in terms of vertical wavenumber, frequency, and horizontal wavenumber. Spectra of the vertical velocity can be related most directly to the spectral properties of the forcing region, which is characterized best by the strong vertical velocities in the tropospheric convective updraft. And while spectra of momentum flux $\rho_0 u'w'$ might better characterize the important property of momentum transport by the waves, vertical velocity spectra can more readily be compared to observations such as those measured by aircraft or radar wind profilers.

1) VERTICAL WAVENUMBER SPECTRA

The PSD of the stratospheric wave field as a function of vertical wavenumber m is shown in Fig. 9. Spectra for the western and eastern halves of the domain are plotted separately. The spectra show a dominant scale of 6–10 km ($m \sim 1$–1.7×10^{-4} Cy m^{-1}), with power falling off steeply at larger wavenumbers following a power law proportional to m^{-4} or m^{-5}. These wavelengths are comparable to the total depth of the troposphere (12 km) in this midlatitude simulation. The shorter wavelengths (<5 km) are nearly absent in the spectrum in Fig. 9, and this property may serve as a signature of waves forced by deep convection. Radar observations of the stratosphere have typically either not resolved waves with vertical wavelengths as large as 10 km, or have filtered these longer vertical scales from their data prior to analysis (e.g., Dewan et al. 1984; Fritts et al. 1988). At a vertical wavelength of 1 km, we can compare the model's stratospheric wave PSD to observations of Dewan et al. (1984), where power spectra of horizontal velocity were determined from rocket smoke trails. PSD in the horizontal velocity field from the simulation at similar heights (not shown) is 2 orders of magnitude smaller than in the observations at $m = 10^{-3}$ Cy m^{-1}. These results suggest observers must focus on longer vertical scales O(10 km)

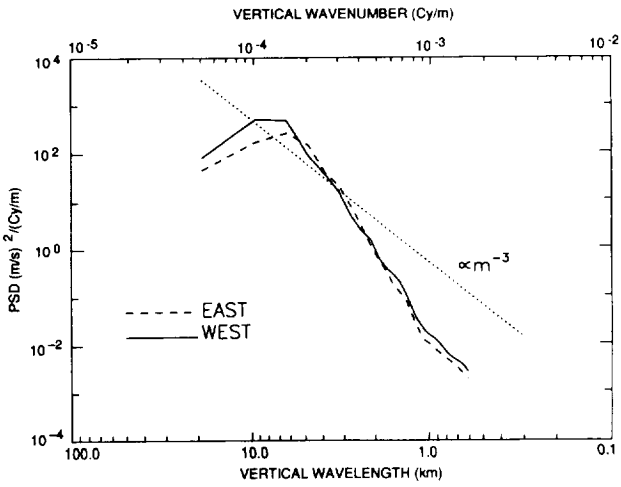

FIG. 9. Power spectrum of the stratospheric vertical velocity field as a function of vertical wavenumber. West and east refer to westward- and eastward-propagating waves as described in the text. The spectrum is strongly peaked at long vertical wavelengths of 6–10 km.

to include waves from this source. Lidar observations (Gardner et al. 1989) suggest vertical wavelengths of 5–10 km are prevalent in the upper stratosphere.

The longer vertical wavelengths are not well resolved in Fig. 9 because of the limited depth of stratosphere in the model ($z \sim 13$–32 km), so the vertical wavelength spectrum does not give much detailed information about the diversity among the stratospheric waves. The spectrum cannot be directly related to an intrinsic zonal phase speed (c_x) spectrum via the hydrostatic relation $c_x = N/m$ because, as will be shown later, much of the spectral power lies in the nonhydrostatic regime.

The vertical wavenumber spectra also illustrate the dominance of waves propagating westward relative to the storm, as described in previous work (Fovell et al. 1992; Holton and Durran 1993). The integrated power in the westward propagating spectrum is a factor of 2 larger than the integrated eastward spectrum. Time loops of the simulation also reveal that the eastward propagating waves in the domain are all forced at early times in the simulation, while conspicuously absent in the near field in the mature squall line (see Figs. 2 and 8).

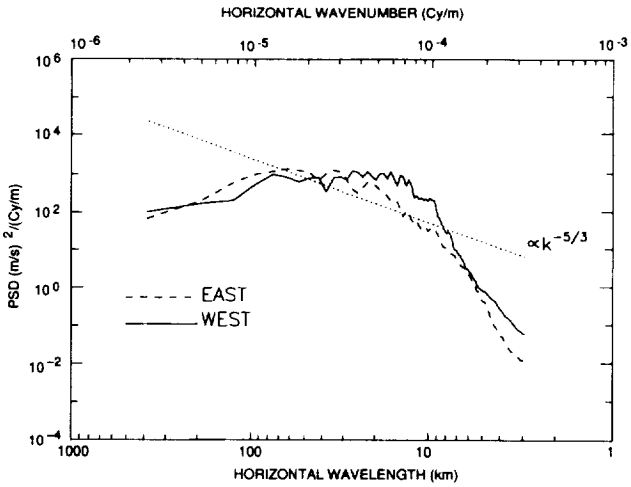

FIG. 10. Power spectrum of the stratospheric vertical velocity field as a function of horizontal wavenumber. West and east refer to westward- and eastward-propagating waves as described in the text. The spectrum is almost featureless for wavelengths in the 10–100-km range that we focus on in our analysis.

2) HORIZONTAL WAVENUMBER SPECTRA

Figure 10 shows the stratospheric domain-averaged power spectra of vertical velocity as a function of horizontal wavenumber k. These power spectra refer to an altitude of 13 km and represent an average over the same region of (x, z, t) as the spectra in Fig. 9. Spectra for regions west and east of the storm center have again been computed separately. Note that similar spectra of the horizontal velocity field (not shown) are comparable or larger in magnitude to observations published in Jasperson et al. (1990) at wavelengths longer than ~10 km. The Jasperson et al. spectra were derived from aircraft measurements during the Global Atmospheric Sampling Program at altitudes just above the tropopause at about 13 km.

The spectra in Fig. 10 show a dominance of waves with horizontal scales between 10 and 100 km that are well resolved in our model. The power spectrum of westward waves is remarkably flat over this interval. Eastward waves are relatively lacking in the shorter wavelengths. A line proportional to $k^{-5/3}$ is also plotted for reference. The Jasperson et al. spectra follow the $k^{-5/3}$ power law over a range of wavelengths from ~3 to 200 km. Comparatively, our spectra of waves generated in the squall line simulations display an absence of power at the long-wavelength end of this range. At the short-wavelength end (<9 km) of the spectrum in Fig. 10, the power drops precipitously because of the numerical smoothing applied to maintain model stability. In previous work (FDH and Holton and Durran 1993), the scale-selective smoothing coefficient $S \equiv K\Delta t/\Delta x^4$ was 2.4–3 times higher, significantly affecting the horizontal wavelength spectrum. Here, K ($m^{-4}\ s^{-1}$) is the biharmonic diffusion coefficient and S is a nondimensional coefficient that turns out to equal one half of the fractional damping per time step for a disturbance of wavelength $4\Delta x$. Holton and Durran (1993) let $S = 0.015$, which as earlier noted strongly damps wavelengths less than 20 km. In this study $S = 0.005$, which is large enough to prevent spurious growth of the $2\Delta x$ and $4\Delta x$ waves but does not significantly damp waves longer than 10 km. The 10–20-km horizontal scale is an important one since convective cell structures often organize in this range (e.g., Houze 1993). In a simulation in which the smoothing coefficient was reduced to $S = 0.002$, there was little change in power for $\lambda_x > 10$ km, but in this case the shortest scales were not sufficiently damped to prevent numerical instability. The numerical smoothing then provides the true horizontal resolution limit in the squall line simulation, so that only waves with wavelengths greater than 10 km can be accurately represented. Changes to the vertical smoothing coefficient, on the other hand, had little effect on the simulation results.

3) FREQUENCY SPECTRA

The stratospheric domain-averaged power spectral density versus intrinsic frequency ω is shown in Fig. 11. This spectrum of the vertical velocity displays the dominance of high-frequency waves with intrinsic periods between ~10 min and 1 h among the westward propagating waves. (Note that the nearly stationary wave described in section 2b, if present in the stratosphere, would not be resolved in this spectrum of

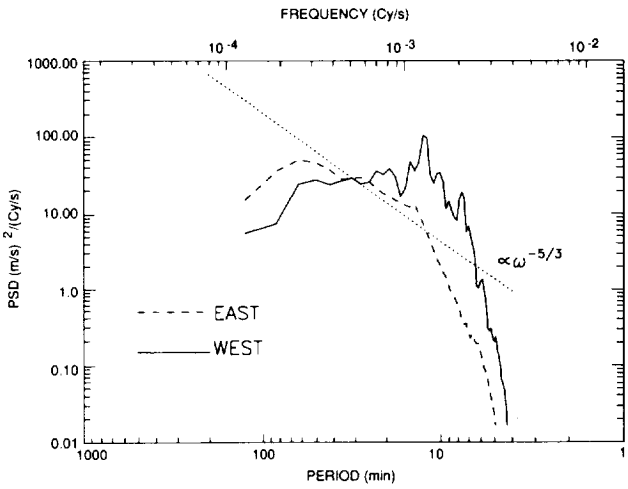

FIG. 11. Power spectrum of the stratospheric vertical velocity field as a function of intrinsic frequency. West and east refer to westward- and eastward-propagating waves as described in the text. High-frequency peaks at 12.8 and 7.8 min stand out prominently in the westward spectrum. These high-frequency responses are associated with the mechanical pumping forcing mechanism that preferentially excites rearward-propagating waves (FDH).

storm-relative frequencies but would appear transient in the ground frame and might have significant variance.) The differences between spectra for the eastward and westward waves are most striking at the higher frequencies, where the east spectrum shows an absence of power at frequencies higher than 1×10^{-3} Cy s^{-1}. Such high frequency waves with eastward storm-relative phase speeds are simply not being forced in the mature storm model. This result is in accord with FDH, if the high-frequency waves are tied to a mechanical pumping/forcing mechanism. Although the total integrated power over the full stratospheric domain only differs by a factor of 2 between east and west, the high-frequency waves carry a disproportionate share of the vertical momentum and energy fluxes. So the westward propagating waves in the simulation are more likely to have an impact on the upper stratosphere and mesosphere. The precipitous drop in power at frequencies higher than 2.4×10^{-3} Cy s^{-1} (~7 min) in the westward spectrum is probably related to the numerical filtering of the short horizontal scales and the weak time filter in the model. In the ground relative frame, the intrinsic periods in Fig. 11 translate to ground relative periods from ~6 min to the 4-h limit of our analysis.

4) TWO-DIMENSIONAL POWER SPECTRA

The power spectra of the westward-propagating waves in Figs. 10 and 11 show that the stratospheric waves are well enough resolved in the horizontal wavenumber and frequency domains to derive the two-dimensional spectrum shown in Fig. 12. Regions of high power denote the ω–k relationships for a given wave mode. The two-dimensional spectrum contains the same information as the two one-dimensional spectra but also provides a crucial link between wavenumber and frequency. With the linear dispersion relation for internal gravity waves, the ω–k relationships can also be related to the important characteristics of vertical wavenumber, phase speed, and group velocity of the stratospheric waves. Figure 12 is limited at low power by the noise in the PSD estimate, which is ~11%. Power is plotted as log(PSD), and the contrast is enhanced to de-emphasize the noise. Focusing on the bright regions with PSD $\geq 10^5$ m^2 s^{-2} (Cy/m)$^{-1}$ (Cy/s)$^{-1}$, patterns are evident that can be explained in the physical context of the wave-forcing mechanisms in the following section. Figure 12 appears blurred for several reasons: (i) the spectral leakage (noise) in the PSD estimate, (ii) the finite resolution limits associated with the limited domain size in x and t ($\Delta k = .02 \times 10^{-4}$ Cy m^{-1}; $\Delta\omega = .06 \times 10^{-3}$ Cy s^{-1}), and (iii) the true variability in the wave field during the course of the simulation resulting from the nonstationarity of the wave forcing in the troposphere.

4. Physical interpretation of the wave spectrum

The regions of highest power in the two-dimensional spectrum in Fig. 12 show organization along preferred lines and curves in the ω–k domain. These can be described in terms of certain fundamental wave characteristics via the linear dispersion relation for internal gravity waves:

$$\omega = \frac{\pm Nk}{\sqrt{k^2 + m^2}}, \qquad (1)$$

the sign depending on whether the waves propagate toward the east or west. Here, ω is the intrinsic frequency, k and m are the horizontal and vertical wavenumbers, respectively, and N is the buoyancy frequency, which is approximately 3.3×10^{-3} Cy s^{-1} throughout the stratosphere. From this relation, relevant wave characteristics such as vertical wavenumber, phase speed, and group velocity can be found for a given (ω, k) pair. Thus, these relevant quantities are uniquely defined at each point in the two-dimensional spectrum in Fig. 12.

In Fig. 13, curves corresponding to three different values of the vertical wavenumber have been superimposed on the two-dimensional power spectrum shown previously in Fig. 12. The three values of m correspond to vertical wavelengths of 4, 8, and 14 km. Observe that most of the power is found in waves with vertical wavelengths between 4 and 14 km. The strongest response is associated with waves having an 8-km vertical wavelength. A weaker secondary maximum is evident at the 4-km vertical wavelength.

The dominance of the 8-km vertical wavelength response appears to be associated with wave forcing due

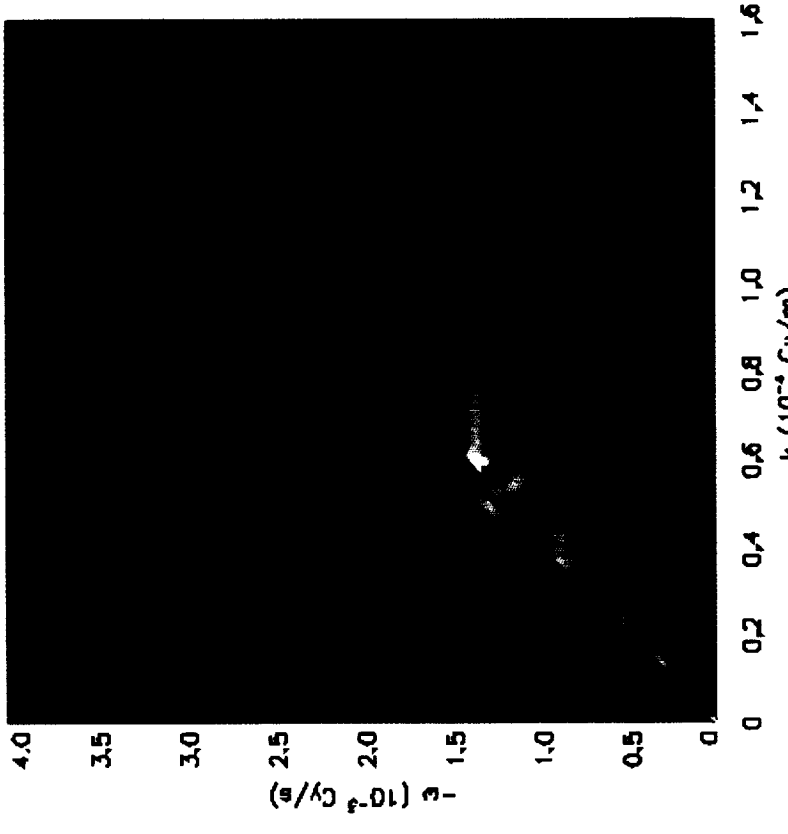

FIG. 13. The 2D power spectrum shown in Fig. 12 overlaid with lines of constant vertical wavelength (long solid lines). From lower to upper curve, these correspond to vertical wavelengths of 4, 8, and 14 km, respectively. The 8-km curve corresponds to the peak in the 1D spectrum in Fig. 9 and shows the stratospheric response to the tropospheric diabatic heating. Two lines of constant frequency equal to 1.3×10^{-3} Cy s^{-1} (12.8 min) and 2.1×10^{-3} Cy s^{-1} (7.8 min) are overlaid as dashed lines. These frequencies correspond to prominent peaks in the 1D spectrum in Fig. 11 and show the stratospheric response to the mechanical pumping mechanism.

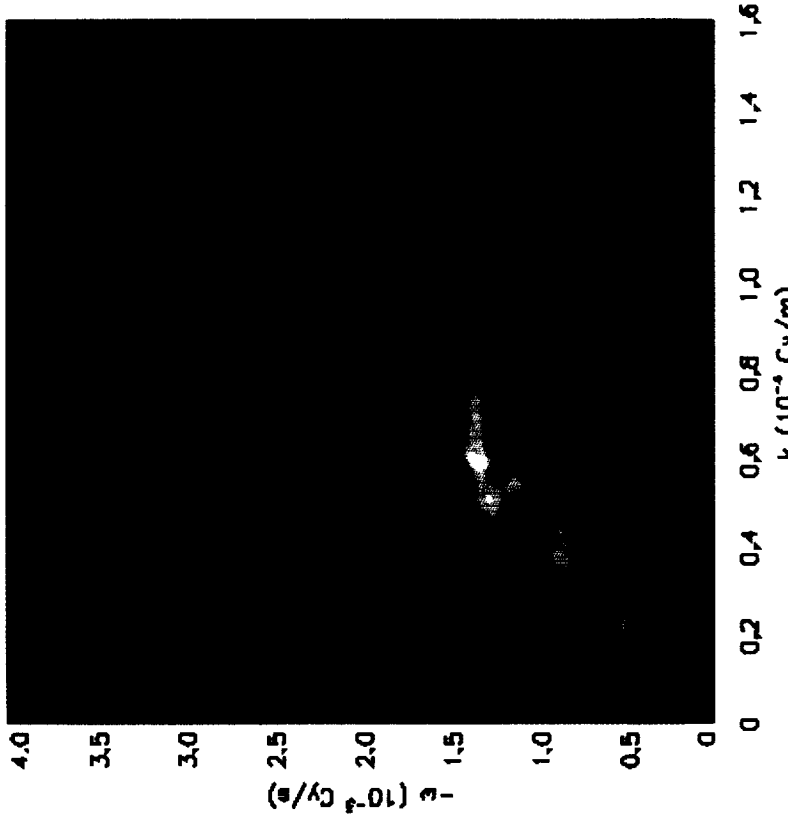

FIG. 12. Two-dimensional power spectrum of the stratospheric vertical velocity field as a function of horizontal wavenumber and intrinsic frequency for the westward-propagating waves.

to latent heating and cooling in the tropospheric updrafts and rain shafts. The linear wave response to a tropospheric heat source has been described by several authors (Lin and Smith 1986; Salby and Garcia 1987; Bretherton 1988; Nicholls et al. 1991; Pandya et al. 1993). According to these earlier studies, the vertical structure of the linear wave response is determined by the vertical structure of the tropospheric heat source. The shape of the tropospheric heating profile in our squall line simulation is similar to the analytical profile chosen by Nicholls et al. (1991, their Fig. 4). The heating is largely confined below an altitude of 8 km. The shape is dominated by a half sine wave function with 16-km vertical wavelength, with overtones of an 8-km wavelength scale also present. These can be visualized from the vertical velocity contours shown in Fig. 3. The change in buoyancy frequency at the tropopause by a factor ~ 2 (Fig. 1b) suggests the vertical wavelength of the stratospheric response would be one-half that of the tropospheric forcing. This follows from (1) in the hydrostatic limit ($m \gg k$) in the absence of shear. Thus, the 16-km and weaker 8-km forcings would correspond to stratospheric responses at vertical wavelengths of 8 km and 4 km, respectively, as observed in the spectrum in Fig. 13.

The above simple relationship may be an oversimplification because there is significant shear in the troposphere and nonhydrostatic effects are important. Further modeling efforts are required to sort out whether these complicating factors affect the above forcing–response vertical wavelength relationship. However, given that the N profile and tropospheric shear are fairly representative of characteristics found in nature, the dominant stratospheric response at a wavelength equal to the depth of the heating is the observable response. Observations of Larsen et al. (1982) and Sato (1993) support this connection between long vertical wavelengths and deep convective heating.

The mechanical oscillator mechanism is also believed to be important in forcing stratospheric waves by deep convection (see FDH). The signature of this mechanism is strongly evident in the power spectrum in Fig. 13 as two prominent horizontal lines at specific frequencies spanning a wide range of horizontal wavenumbers. This response appears to be related to the oscillation of peak vertical velocity in the central updraft and to the formation of new convective cells, shown in Fig. 14a. Peak vertical velocity in the core of the storm (W_{PEAK}) is plotted as a function of time, as well as the altitude of the peak (Z_{PEAK}). Lag correlations (Fig. 14b) of these time series show that both the altitude and amplitude of the peak updraft oscillate with a pronounced periodicity of ~25–27 min. Cross correlation shows W_{PEAK} leads Z_{PEAK} by 2 min. The power spectrum of W_{PEAK} (shown in Fig. 15 as the solid curve) displays dominant power at periods near 23–28 min and a secondary peak near 13 min. The time series in Fig. 14 describe the vertical velocity amplitude and altitude of new "convective cells" as they form. The cells appear as centers of strong vertical velocity perturbation. The perturbations tend to appear at low altitudes (~3 km) in the troposphere, then rise as they grow in amplitude and propagate rearward relative to the storm center. Their amplitudes fall sharply, however, before they reach peak altitude. Both time series later begin to track the next newly formed cell. The 2-min lag in the Z_{PEAK}–W_{PEAK} cross correlation shows that amplitude falls sharply before the next new large-amplitude cell forms at lower altitudes. The oscillations in Z_{PEAK} suggest the average cell-formation period is 16 min, with a 23-min spacing most common and a 12-min period a close second. Vertical velocity amplitudes, on the other hand, oscillate most prominently on the longer timescale. The spectrum of vertical velocity at single points in the upper troposphere (dotted curve

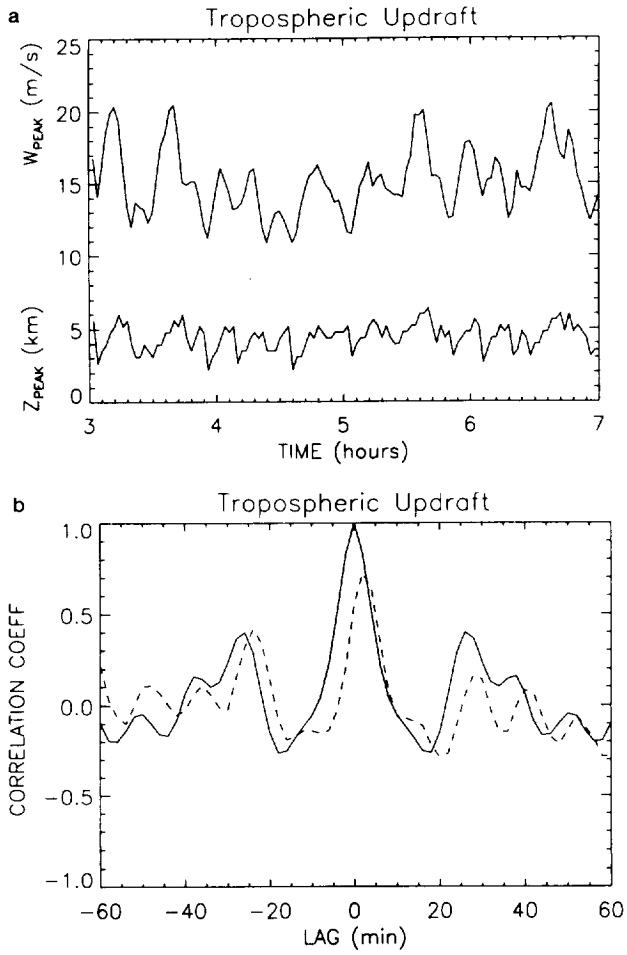

FIG. 14. (a) Time history of the peak vertical velocity near storm center (W_{PEAK}) and the altitude at which the peak occurs (Z_{PEAK}). (b) Autocorrelation of W_{PEAK} (solid line) showing the prominent 26-min period of oscillation. Cross correlation of W_{PEAK} and Z_{PEAK} (dashed line) shows these are highly correlated, with W_{PEAK} leading Z_{PEAK} by 2 min.

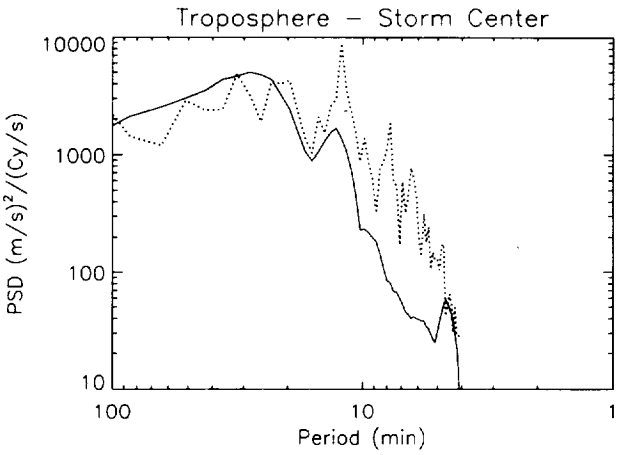

FIG. 15. Power spectrum of W_{PEAK} (solid line) shows the dominance of longer-period (23–28 min) oscillations emphasized by the correlation analysis (Fig. 14b). [Note this spectrum of the single time series (Fig. 14a) has been smoothed to reduce the standard deviation to 30%.] The dotted line shows the spectrum of vertical velocity at fixed points in the upper troposphere (z = 6–12 km) at storm center that have been spatially averaged to reduce the standard deviation to 6%. This spectrum more resembles the stratospheric spectrum shown in Fig. 11 where short-period signals ($\leq$13 min) dominate. The long-period oscillations associated with the forcing are not so prevalent, but short-period responses at 7.8 and 6.4 min appear and are associated with harmonics of the long period of the forcing.

in Fig. 15) shows many similarities to the stratospheric spectrum (Fig. 11), except that the longer period waves are of a much lower amplitude in the stratosphere relative to the 12–13-min peak. A peak at 7.8 min also stands out above the noise in both the stratosphere and upper-troposphere spectra. These two peaks in the spectrum are associated with horizontal lines of high power in the 2D spectrum that are highlighted with dashed lines in Fig. 13. This type of spectral response is what would be expected from the mechanical oscillator mechanism described in FDH. Mechanical pumping at a given frequency will generate waves at that characteristic frequency but with a range of wavelengths related to the spectral shape of the oscillator in the spatial dimension x and, hence, straight horizontal lines in Fig. 13.

The high-frequency peaks in the stratosphere at 12.8 and 7.8 min correspond fairly well to the first and second harmonics of a fundamental oscillation with a period of 23–26 min. This suggests that the prominent oscillation in W_{PEAK} in the troposphere may be demonstrating this fundamental oscillation period, while the stratospheric waves demonstrate the response to this forcing. It may also be relevant that there are nonlinear resonances between a period of 12–13 min and periods in the 23–28-min range. A response at 7.7–8.8 min would also result from such interactions. Further work on this subject, including comparisons to linear models, is necessary before any firm conclusions about these forcing mechanism details can be made. Some of the more energetic of the propagating cells in the trailing-cloud region may also be acting as secondary centers of this mechanical pumping mechanism.

The broad response in k along these constant ω lines should be related to the shape in x of the oscillator. The vertical velocity profile in x of the main updraft, $w(x)$, has a Gaussian shape with a narrow half width of ~7 km. The Fourier transform of a sharply peaked Gaussian is a broad Gaussian in wavenumber (k) centered at zero. A Gaussian fit to the power spectrum of the central updraft $w(x)$ (not shown) gave a half width of $\sim 0.8 \times 10^{-4}$ Cy m^{-1}, which can explain the decrease in power at the high-k end of these constant ω lines. Some other process limits the response at the low-k end, which is not yet fully understood. Both the response to the mechanical oscillator forcing and the response at the longest vertical wavelengths (~14 km) seem to be limited to vertical group velocities less than 15–20 m s^{-1}. This limit in the spectrum may reflect the inability to clearly see these waves in the power spectrum if they are forced only sporadically, since a wave packet with that group velocity would traverse the entire stratospheric domain in only 15–20 min.

The presence of these lines at constant ω in the spectrum are a clear indication of the mechanical pumping mechanism active in forcing the stratospheric waves. The specific frequencies associated with each harmonic suggest prominent phase lines lie at precise angles from the vertical equal to 67° and 50°. The mechanical pumping mechanism forces only westward propagating waves, primarily because of the westward motion of the rising convective cells in the center of the storm (FDH). Future work will study the momentum deposition and mean flow forcing in the middle atmosphere of all the waves generated in the simulation for realistic mean wind profiles.

5. Conclusions

The squall line model has been shown to force a rich spectrum of vertically propagating gravity waves. The model has high enough resolution and a domain large enough to spectrally characterize the stratospheric waves. The spectral analysis of section 3 sufficiently characterizes the spectral properties of the waves to define their frequencies, wavenumbers, phase speeds, and group velocities. Figure 12 and the linear dispersion relation provides the information needed for future studies of their propagation in the interactions with realistic middle atmosphere wind profiles.

The spectrum also points to specific forcing mechanisms active in the model, which are described in section 4. Each mechanism by its physical nature places natural limits on the spectral response. Thus, identification of the specific spectral signature associated with each forcing mechanism points to its presence in the simulation, and the power in the spectrum matching each signature gives its relative importance to the total wave field.

The description of the gravity wave forcing in section 4 is consistent with the results of the spectral analysis, with our knowledge of the behavior of the storm, with simulations by other authors, and with observations where they exist. The conclusions are still fairly qualitative in nature, but provide a guide for future quantitative modeling with simpler linear models to demonstrate the forcing mechanisms in more detail. Although the results are specific to the squall line simulation being studied, we can make some general statements regarding the spectrum of vertically propagating waves generated by long-lived deep convection. Given the forcing mechanisms described in section 4, the response is largely governed by three properties of the storm: 1) the depth of the diabatic heating layer, 2) the oscillation frequency of the main updraft, and 3) the storm propagation speed. The depth of the heating largely determines the vertical wavenumber of the wave response. The oscillation frequency of the central updraft of the storm determines the intrinsic frequencies of waves forced via the mechanical pumping mechanism. Then ground relative frequencies and phase speeds follow from the above properties and the speed of the storm via the Doppler relationship. Such a description of the wave field in terms of these fundamental properties provides a first step toward a parameterization of waves forced in deep convection, though there are still many questions left to be answered.

First, there are obvious limits in frequency and/or horizontal wavenumber evident in Fig. 13 that are not well determined by the forcing mechanisms outlined in section 4. What provides the low-k limit for waves forced via the mechanical pumping mechanism? How will other buoyancy frequency and wind profiles modify the vertical wavelength response in the stratosphere? What provides the high-ω limit to the stratospheric response at the longest vertical wavelengths $\lambda_z \sim 14$ km? Comparison of the nonlinear storm model with idealized linear models of the forcing mechanisms may illuminate some of these limits and will also provide an evaluation of any nonlinear forcing effects on the stratospheric wave spectrum. The frequency of oscillation of the tropospheric updraft determines the spectral properties of waves forced by the mechanical pumping mechanism. In this storm simulation one particular frequency dominates; however, the meteorological conditions determining this frequency are not well understood (Fovell and Ogura 1989), nor is there much constraining observational evidence. Observed cases of multicell storms suggest new cell formation occurs at periods of roughly 5–30 min.

The rather regular tropospheric oscillations in the mature storm in our simulation may not be representative of such storms in nature. In fact, we find the simulations can be quite sensitive to the model conditions, such that the steady oscillations are replaced by more chaotic behavior, in general agreement with the conclusions of Fovell and Dailey (1995). The statistically steady case we have examined here lends itself to identification of the spectral response to the active forcing mechanisms in the model. Presumably, the same forcing mechanisms are active in the more chaotic cases; however, interpretation of the spectrum cannot be made so clearly. Examination of a broader range of storm conditions and responses, however, may provide a more general picture of the characteristics of the stratospheric waves produced in a statistical sense. Future work must also include modeling of tropical convection cases and extensions to three dimensions to test the robustness and generality of the conclusions.

Observational verification of the nature of waves associated with convection is also needed. Several observable characteristics of the convectively generated waves have been outlined here, which may serve as signatures of their origin. Verification by observation would provide a test of some of the predictions of the wave properties described here. Specifically, the prevalence of long vertical wavelengths approximately equal to the depth of the heating (Figs. 9 and 13) is a prominent feature of the waves in the model. These longer wavelengths are often unresolved or filtered out in observational analyses. The Aericibo radar observations of wave motions above deep convective clouds in Larsen et al. (1982) are in good agreement with our model results. The asymmetry in the momentum flux ahead of versus behind the storm (Fig. 8) is another prominent feature of the stratospheric waves that may be observable by ground-based radar systems or in high-flying-aircraft wind data. Finally, the nearly stationary wave (in storm-relative coordinates) observed in the upper troposphere (Figs. 5–7) may be a common feature of deep convection, as evidenced in the Balsley et al. (1988) vertical wind profiler observations and the MU radar observations of Sato (1993). Further observations of multicell storms might also provide some measure of typical frequencies associated with the formation of new convective cells, which we have shown will characterize a significant portion of the wave spectrum.

Acknowledgments. This work was supported by the Physical Meteorology Program of the National Science Foundation under Grant ATM-8813971 and NASA under Grant NAGW-662. The authors would like to thank Dr. Robert Vincent for valuable discussions regarding observational verification of the simulation results and Drs. Kaoru Sato and Miguel Larson for pointing out some important comparisons to radar observations. We also thank Louisa Nance for identifying a problem associated with high scale-selective smoothing in the model, Ming Jen Yang for editing comments, and Rajul Pandya for his analysis of the heating function in the simulation. Dr. Rob Fovell and two anonymous reviewers provided valuable editorial comments.

REFERENCES

Bacmeister, J. T., 1993: Mountain-wave drag in the stratosphere and mesosphere inferred from observed winds and a simple mountain-wave parameterization scheme. *J. Atmos. Sci.*, **50,** 377–399.

Balsley, B. B., W. L. Ecklund, D. A. Carter, A. C. Riddle, and K. S. Gage, 1988: Average vertical motions in the tropical atmosphere observed by a radar wind profiler on Pohnpei (7°N latitude, 157°E longitude). *J. Atmos. Sci.*, **45,** 396–405.

Bergman, J. W., and M. L. Salby, 1994: Equatorial wave activity generated by fluctuations in observed convection. *J. Atmos. Sci.*, **51,** 3791–3806.

Bretherton, C., 1988: Group velocity and the linear response of stratified fluids to internal heat or mass sources. *J. Atmos. Sci.*, **45,** 81–93.

Dewan, E. M., N. Grossbard, A. F. Quesada, and R. E. Good, 1984: Spectral analysis of 10m resolution scalar velocity profiles in the stratosphere. *Geophys. Res. Lett.*, **11,** 80–83; Correction, 624.

Dunkerton, T. J., 1982: Theory of the mesopause semiannual oscillation. *J. Atmos. Sci.*, **39,** 2681–2690.

Durran, D. R., 1994: Does mountain wave drag decelerate the local flow? *J. Atmos. Sci.*, submitted.

——, and J. B. Klemp, 1983: A compressible model for the simulation of moist mountain waves. *Mon. Wea. Rev.*, **111,** 2341–2361.

——, M.-J. Yang, D. N. Slinn, and R. G. Brown, 1993: Toward more accurate wave-permeable boundary conditions. *Mon. Wea. Rev.*, **121,** 604–620.

Fovell, R. G., and Y. Ogura, 1989: Effect of vertical wind shear on numerically simulated multicell storm structure. *J. Atmos. Sci.*, **46,** 3144–3176.

——, and P. S. Dailey, 1994: The temporal behavior of numerically simulated multicell-type storms. Part I: Modes of behavior. *J. Atmos. Sci.*, **52,** 2117–2139.

——, D. Durran, and J. R. Holton, 1992: Numerical simulations of convectively generated stratospheric gravity waves. *J. Atmos. Sci.*, **49,** 1427–1442.

Fritts, D. C., and R. A. Vincent, 1987: Mesospheric momentum flux studies at Adelaide, Australia: Observations and a gravity wave–tidal interaction model. *J. Atmos. Sci.*, **44,** 605–619.

——, and G. D. Nastrom, 1992: Sources of mesoscale variability of gravity waves. Part II: Frontal, convective, and jet stream excitation. *J. Atmos. Sci.*, **49,** 111–127.

——, T. Tsuda, T. Sato, S. Fukao, and S. Kato, 1988: Observational evidence of a saturated gravity wave spectrum in the troposphere and lower stratosphere. *J. Atmos. Sci.*, **45,** 1741–1759.

Garcia, R. R., and S. Solomon, 1985: The effect of breaking gravity waves on the dynamics and chemical composition of the mesosphere and lower thermosphere. *J. Geophys. Res.*, **90,** 3850–3868.

Gardner, C. S., M. S. Miller, and C. H. Liu, 1989: Rayleigh lidar observations of gravity wave activity in the upper stratosphere at Urbana, Illinois. *J. Atmos. Sci.*, **46,** 1838–1854.

Holton, J. R., 1983: The influence of gravity wave breaking on the general circulation of the middle atmosphere. *J. Atmos. Sci.*, **40,** 2497–2507.

——, and D. Durran, 1993: Convectively generated stratospheric gravity waves: The role of mean wind shear. *Coupling Processes in the Lower and Middle Atmosphere,* E. V. Thrane, T. Blix, and D. Fritts, Eds., Kluwer Academic, 175–189.

Houze, R. A., Jr., 1993: Mesoscale Convective Systems. *Cloud Dynamics,* Academic Press, 348–394.

Jasperson, W. H., G. D. Nastrom, and D. C. Fritts, 1990: Further study of terrain effects on the mesoscale spectrum of atmospheric motions. *J. Atmos. Sci.*, **47,** 979–987.

Larsen, M. F., W. E. Swartz, and R. F. Woodman, 1982: Gravity-wave generation by thunderstorms observed with a vertically-pointing 430 MHz radar. *Geophys. Res. Lett.*, **9,** 571–574.

Lin, Y. L., and R. B. Smith, 1986: Transient dynamics of airflow near a local heat source. *J. Atmos. Sci.*, **43,** 40–49.

Lu, D., T. E. VanZandt, and W. L. Clark, 1984: VHF Doppler radar observations of buoyancy waves associated with thunderstorms. *J. Atmos. Sci.*, **41,** 272–282.

McFarlane, N. A., 1987: The effect of orographically excited gravity wave drag on the general circulation of the lower stratosphere and troposphere. *J. Atmos. Sci.*, **44,** 1775–1800.

Nicholls, M. E., R. A. Pielke, and W. R. Cotton, 1991: Thermally forced gravity waves in an atmosphere at rest. *J. Atmos. Sci.*, **48,** 1869–1884.

Palmer, T. N., G. J. Shutts, and R. Swinbank, 1986: Alleviation of a systematic westerly bias in general circulation and numerical weather prediction models through an orographic gravity wave drag parameterization. *Quart. J. Roy. Meteor. Soc.*, **112,** 1001–1039.

Pandya, R., D. Durran, and C. Bretherton, 1993: Comments on "Thermally forced gravity waves in an atmosphere at rest." *J. Atmos. Sci.*, **50,** 4097–4101.

Percival, D. B., and A. T. Walden, 1993: *Spectral Analysis for Physical Applications.* Cambridge University Press, 583 pp.

Pfister, L., 1986: Small-scale motions observed by aircraft in the tropical lower stratosphere: Evidence for mixing and its relationship to large-scale flows. *J. Atmos. Sci.*, **43,** 3210–3225.

——, S. Scott, M. Loewenstein, S. Bowen, and M. Legg, 1993a: Mesoscale disturbances in the tropical stratosphere excited by convection: Observations and effects on the stratospheric momentum budget. *J. Atmos. Sci.*, **50,** 1058–1075.

——, K. R. Chan, T. P. Bui, S. Bowen, M. Legg, B. Gary, K. Kelly, M. Proffitt, and W. Starr, 1993b: Gravity waves generated by a tropical cyclone during the STEP tropical field program: A case study. *J. Geophys. Res.*, **98,** 8611–8638.

Press, W. H., B. P. Flannery, S. A. Teukolsky, and W. T. Vetterling, 1989: *Numerical Recipes: The Art of Scientific Computing.* Cambridge University Press, 702 pp.

Rind, D., R. Suozzo, N. K. Balachandran, A. Lacis, and G. Russell, 1988: The GISS global climate–middle atmosphere model. Part I: Model structure and climatology. *J. Atmos. Sci.*, **45,** 329–370.

Rotunno, R., J. B. Klemp, and M. L. Weisman, 1988: A theory for strong, long-lived squall lines. *J. Atmos. Sci.*, **45,** 463–485.

Salby, M. L., and R. R. Garcia, 1987: Transient response to localized episodic heating in the tropics. Part I: Excitation and short-time near-field behavior. *J. Atmos. Sci.*, **44,** 458–498.

Sato, K., 1993: Small-scale wind disturbances observed by the MU radar during the passage of Typhoon Kelly. *J. Atmos. Sci.*, **50,** 518–537.

Takahashi, M., and B. A. Boville, 1992: A three-dimensional simulation of the equatorial quasi-biennial oscillation. *J. Atmos. Sci.*, **49,** 1020–1035.

Vincent, R. A., and I. M. Reid, 1983: HF Doppler measurements of mesospheric gravity wave momentum fluxes. *J. Atmos. Sci.*, **40,** 1321–1333.

Weisman, M. L., and J. B. Klemp, 1982: The dependence of numerically simulated convective storms on vertical wind shear and buoyancy. *Mon. Wea. Rev.*, **110,** 504–520.

Yang, M.-J., and R. A. Houze Jr., 1994: Multicell squall line structure as a manifestation of vertically trapped gravity waves. *Mon. Wea. Rev.*, **123,** 641–661.